

On the Spray Forming of Metals,
the Formation of Porosity and
the Heat Evolution during Solidification

José Tinoco

November 2003
Doctoral Thesis
Royal Institute of Technology
Casting of Metals
S-100 44 Stockholm, Sweden

Akademisk avhandling som med tillstånd av Kungliga Tekniska Högskolan i Stockholm framlägges till offentlig granskning för avläggande av teknologie doktorsexamen fredagen den 14:de november 2003 kl 13.15 i Sal B2, Kungliga Tekniska Högskolan, Brinellvägen 23, Stockholm.

©José Tinoco

Stockholm 2003 ISSN-1104-7127 / TRITA-MG 2003:03

On the Spray Forming of Metals, the Formation of Porosity and the Heat Evolution during Solidification

José Tinoco

Casting of Metals

Royal Institute of Technology

S-100 44 Stockholm, Sweden

Abstract

This thesis deals with the heat evolution during solidification and its relation to the formation of porosity. It intends to improve the current understanding of the formation of porosity in cast materials with special interest in nodular cast iron and the spray forming process. Two different systems, a Fe-based alloy, Cast iron, and a Ni-based alloy, Inconel 625, are examined. The effect on the heat evolution of the morphology and the processing parameters in spray forming are treated.

An evaluation of the microstructural features, segregation behavior and physical properties such as latent heat of fusion is performed by using thermal analysis under cooling rates ranging from 0.1 to 10^4 K/s. In order to achieve this a modified differential thermal analysis (DTA) equipment, a mirror furnace and levitation casting are used. Results are presented in terms of the fraction of solidified, the cooling rate and the microstructure observed. The measured latent heat of fusion is not constant throughout the solidification process. Variations in morphology and cooling rate affect the release of the latent heat.

A thermodynamic model is used to describe the experimental observations and to explain the formation of pores in nodular cast iron by taking into consideration the formation of lattice defects during the liquid/solid transformation. In this case the formation of porosity is regarded as a consequence of changes in the volume fraction ratio graphite/ γ during the solidification process.

A numerical model of the spray forming process is developed by means of CFD modelling and compared with experimental measurements performed in an industrial facility. Stagnation pressure measurements provided information about the gas flow velocity and an analysis of the overspray powder provided information about the particle thermal history. Evaluation of the deposit was also performed. It is observed that the process conditions in spray forming promote non-equilibrium solidification even though solidification at the deposit occurs at a lower rate. In this case the porosity formed near the interface substrate/deposit depends largely on the substrate temperature. The presence of certain reactive elements, such as titanium, affects the porosity levels in the rest of the deposit.

Descriptors: *Thermal Analysis, Nodular Cast Iron, Inconel 625, CFD, Flow Assessment, Multiphase Flow, Spray Deposition, Microporosity, Superalloys*

This thesis is based on the following supplements:

Supplement 1. J. Tinoco and H. Fredriksson, 'On the solidification behavior of nodular cast iron', Proceedings of the International Conference "The Science of Casting and Solidification", Brasov, Rumania, 305-311 (2001)

Supplement 2. J. Tinoco, P. Delvastio, O. Quintero and H. Fredriksson, 'Thermal analysis of nodular and lamellar eutectic cast iron under different cooling rates', International Journal of Cast Metals, Vol. **16** No. 1-3 (2003)

Supplement 3. H. Fredriksson, J. Stjerndahl and J. Tinoco, 'On the expansion and contraction of nodular cast iron', ISRN-KTH: MG-INR-03:05se, TRITA-MG 2003:05, Royal Institute of Technology, Stockholm, Sweden, Oct. (2003)

Supplement 4. J. Tinoco and H. Fredriksson, 'Solidification of a modified Inconel 625 under different cooling rates', accepted for publication in High Temperature Materials and Processes, Sept. (2003)

Supplement 5. J. Tinoco, B. Widell, H. Fredriksson and L. Fuchs, 'Modelling the in-flight events during metal spray forming', in press in Materials Science and Engineering A, Nov. (2003)

Supplement 6. J. Tinoco, B. Widell and H. Fredriksson, 'Fluid flow studies in a metal spray deposition chamber. CFD model and validation', accepted for publication in Materials Science and Engineering A, Sept. (2003)

Supplement 7. J. Tinoco and H. Fredriksson, 'Metal spray deposition of cylindrical preforms', ISRN-KTH: MG-INR-03:06se, TRITA-MG 2003:06, Royal Institute of Technology, Stockholm, Sweden, Oct. (2003)

...where there is a will there is a way

Reinhold Meisner

Contents

1	Introduction	3
1.1	Background	3
1.2	Aim and scope	4
1.3	Outline	4
2	Thermal analysis	5
2.1	Experimental techniques	5
2.1.1	Differential thermal analysis (DTA)	5
2.1.2	Mirror furnace technique	5
2.1.3	Levitation casting	5
2.2	Results	6
2.2.1	Segregation behavior	6
2.2.2	Phase volume fraction	7
2.2.3	Structure evolution	8
3	Heat of fusion	11
3.1	Heat transfer model	11
3.2	Results	12
3.3	Advantages and disadvantages	12
4	Volume change and porosity	15
4.1	Thermodynamic considerations	15
4.2	Growth rate	17
5	Spray forming	19
5.1	Plant trials	19
5.1.1	Flow assessment	20
5.1.2	Particle state analysis	20
5.1.3	Structure in the deposit	21
5.2	Numerical simulations	21
5.2.1	CFD model	22
5.2.2	Deposition	25
5.3	Model validation	27
6	Concluding remarks	31
	Bibliography	33
	Acknowledgements	35

Chapter 1

Introduction

1.1 Background

The properties of metal castings are mostly determined by the conditions which control the solidification process. Nowadays the demands on quality and properties of the cast materials have increased tremendously. In order to meet such demands the control of the processing of the material must be continuously improved. Casting defects such as porosity become less than unacceptable in cast products. The porosity arises mainly as consequence of the evolution of gas in the liquid-solid interface, the change in density between liquid and solid state during solidification or the inherent conditions of the process by which the material is produced.

During any solidification process latent heat of fusion is released. The heat of fusion represents the energy required for melting a mass unit or a mole of the substance, i.e. total energy needed to break the bonds between the atoms in the crystal lattice. It has been shown by means of thermal analysis that the latent heat for nodular cast iron is smaller than that of grey cast iron [1]. From an equilibrium point of view the two different solidification modes should have given the same value. In recent studies it was also observed that the heat of fusion decreases as a function of cooling rate [2] [3] [4] [5]. One hypothesis, which can explain this, is that defects, such as vacancies, are formed at the solidification front during the solidification process. If vacancies are present, some bonds are missing and thus the energy difference between the solid and the liquid state decreases with increasing vacancy concentration [6].

On one hand, the porosity appears to be related to the morphology of precipitating phases. A particular example is cast iron. Graphite precipitation in cast iron can occur in a number of shapes depending mostly on the levels of sulfur and active elements as magnesium or cerium [7]. When in cast iron graphite precipitates as nodules two types of shrinkage pores are usually observed [8] [9] [10] [11]. One type is formed by the shrinkage during the initial period of the solidification process [10]. Those pores are usually called macro pores and they can be filled by a riser. The other type of pores, usually called micro pores, is formed in the end of the solidification.

On the other hand, the manufacturing process by which the material is produced or cast also plays an important role in the formation of porosity. An interesting case is the spray forming process. In this kind of process molten metal is atomized by using high velocity gas. The spray formed is deposited onto a substrate and a near-net shape is formed. Near net-shape products are generated in one integrated operation, this represents significant economic benefit compared to ingot and powder manufacturing. Porosity in spray forming represents a major drawback [12] [13]. The increase of the yield by reducing the porosity requires a good understanding of how the structure develops along the entire process.

1.2 Aim and scope

This work intends to increase the understanding of the heat evolution during solidification and its dependence on variables describing the morphology of the precipitating phases and the kinetics of the process. Furthermore it provides a framework in which improved understanding of the formation of porosity in cast materials process can be obtained.

In this thesis two different systems, a Fe-based alloy, Cast iron, and a Ni-based alloy, Inconel 625, will be examined. Throughout this work, the effect on the heat evolution of the morphology and the processing parameters in spray forming will be treated.

1.3 Outline

The outline of this thesis is schematically represented in Figure 1.1. It is divided into four parts which are interconnected and not necessarily presented chronologically. The first part deals with the evaluation and analysis of the solidification behavior of the material by using thermal analysis. In this part results concerning structure evolution, segregation behavior and precipitation of phases for both alloys are presented. The second part presents a heat transfer model for the evaluation of the heat of fusion together with results obtained in terms of fraction solidified and cooling rate. In the third section the volume change during solidification is related to the formation of porosity in the Fe-based alloy. In order to achieve this, thermodynamic calculations are used to derive a growth rate model for one of the precipitating phases involved in the solidification. The fourth and last part focuses on an assessment of the spray forming of tubular preforms of the Ni-based alloy. This is carried out by performing plant trials in an industrial facility together with numerical simulations. In this section numerical modelling is used to investigate the heat transfer conditions occurring along the different stages of the process. This thesis comprises somehow a brief presentation of a series of freestanding reports which are included as supplements at the end of this document.

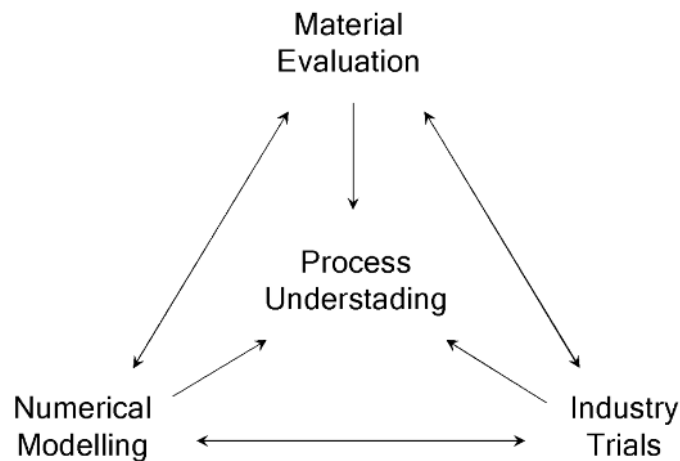


Figure 1.1: Outline of the thesis

Chapter 2

Thermal analysis

2.1 Experimental techniques

Thermal analysis was first used for determination of physical and chemical properties of materials in 1830 when Rudberg [14] made his first thermal analysis of lead-tin alloys by using a mercury thermometer. The main advantage of this technique lies on the fact that it provides a way to study the solidification process and to predict the final microstructure of the alloy. In this chapter, a thermal analysis study of the solidification process under different cooling rates is presented. Three different variations of this experimental technique were used during the performance of this study, a brief description of them is given below. The purpose was to melt and cool down samples in a controlled manner under cooling rates ranging from 0.1 K/s to 10000 K/s.

2.1.1 Differential thermal analysis (DTA)

Samples weighting between 4 and 6 gr are contained in ceramic crucibles. During the experiments a graphite cylinder surrounds the sample crucible. The experiments are performed in an electric resistance furnace under an argon atmosphere. The temperature of both the sample and the graphite cylinder are collected by a PC data acquisition system with a sampling rate of 1 Hz. Quench-out experiments were made along the solidification sequence of the alloy. Figure 2.1(a) shows a description of the set up. Typical cooling curves are presented in supplement 1, 2, 3 and 4.

2.1.2 Mirror furnace technique

Samples of about half a gram are contained in a thin-walled quartz tube. A thermocouple is located at the center of the sample. The tube is evacuated before is sealed and tested. The sample is located in the focal point of two halogen lamps. The temperature is controlled by the power supply to the lamps and registered during the test with a sampling rate of 100 Hz. Figure 2.1(b) shows a schematic representation of the set up. Typical cooling curves are presented in supplement 2 and 4.

2.1.3 Levitation casting

In this case a special shaped coil is made of $\varnothing 3$ mm copper tube. The coil is coupled to a high induction transformer which controls the current. A magnetic field is induced by the current

passing through the coil. The magnetic field has two purposes, first to induce a lifting force and secondly to melt the sample, both simultaneously. Under an argon atmosphere the sample of about half gram levitates and reaches the required superheat. Then, by turning off the power the droplet falls freely into a slim cavity made in a cooper mold where an open thermocouple is placed. Temperature readings are collected with a sampling rate of 3500 Hz. Figure 2.1(c) shows a schematic representation of the set up. Typical cooling curves are presented in supplement 4.

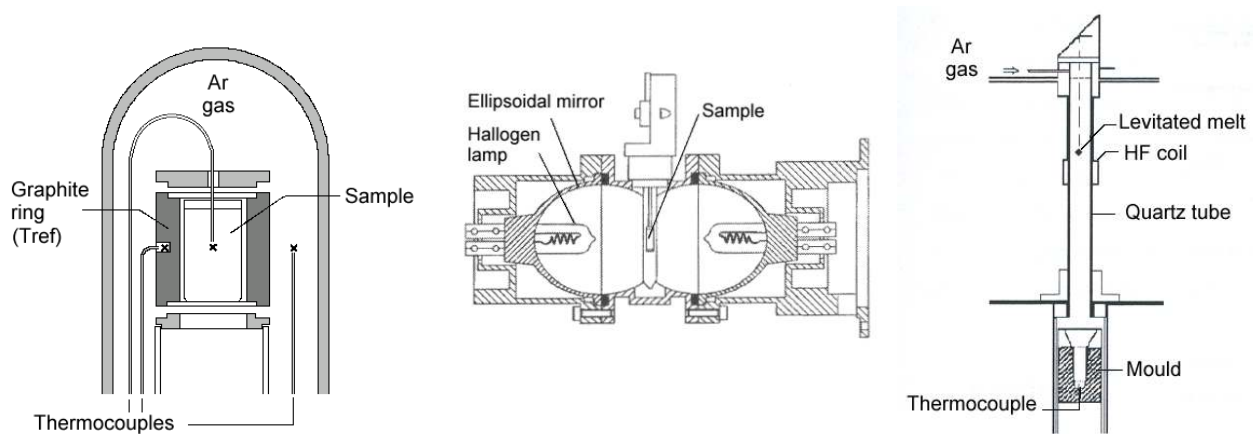


Figure 2.1: (a) DTA (b) Mirror furnace [15] (c) Levitation casting [5]

2.2 Results

In this section results from the evaluation of the two materials are presented; the Fe-based alloy, eutectic cast iron with flake and nodular graphite and the Ni-based alloy Inconel 625. These results are presented into three categories: segregation behavior, phase volume fraction and structure evolution

2.2.1 Segregation behavior

Various alloy elements have different partition coefficients and different tendencies for segregation. For example in Inconel 625 molybdenum and niobium segregates in a positive manner while chromium segregates inversely, i.e. its content decreases towards the outer regions of the dendrite. In order to describe the tendency for segregation the concept of degree of segregation has been introduced, that is the ratio between the highest and lowest measured value of the concentration of the alloy element. Accordingly the ratio between the lowest measured value and the nominal value in the alloy has also been used as an indication of the segregation behavior. Figure 2.2 shows the segregation ratio for different elements present in Inconel 625. It is known that niobium segregates strongly in this alloy [16], thus it can be used to illustrate the behavior of the material. As it is shown the degree of segregation for niobium decreases as the cooling rate increases. This reflects the fact that the increase in cooling rate and corresponding decrease in local solidification time reduces the time available for back diffusion.

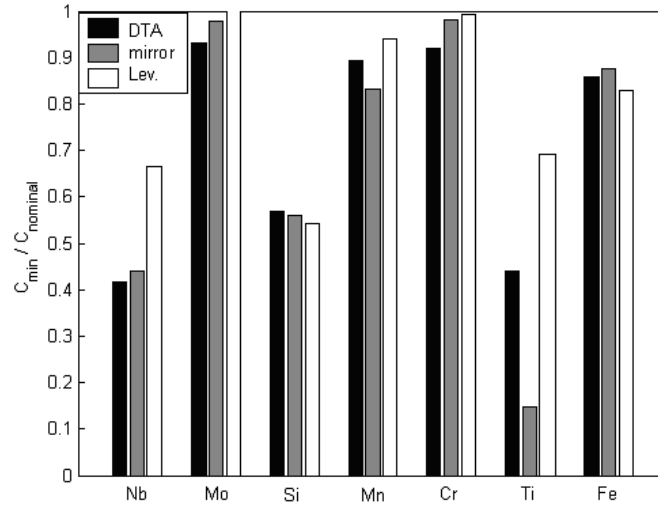


Figure 2.2: Minimum concentration measured in the dendrite core in alloy 2 samples

2.2.2 Phase volume fraction

This section presents information concerning the phases which precipitate in the material.

Cast Iron

In the case of cast iron mainly two phases austenite and graphite are found apart from liquid during solidification. The austenite can precipitate as independent dendrites and/or forming an eutectic aggregate with graphite. The morphology of this aggregate depends mostly on the shape of the graphite. When graphite precipitates as flakes the eutectic aggregate looks like a rosette, the two phases grow side by side into the liquid. When graphite grows as a nodule one of the phases forms a shell around the other. This can be observed in figure 2.3a.

According to the equilibrium phase diagram at the eutectic point, the volume fraction ratio graphite/ γ should be equal to 0.115 ($\rho_\gamma = 7.87 \text{ gr/cm}^3$ and $\rho_{\text{graphite}} = 1.5 \text{ gr/cm}^3$). This value is presented in figure 2.4 together with the measured values of volume fraction ratio. In the figure the ratio represents the total volume fraction of austenite (the sum of the austenite in the dendrites and in the shell) divided by the volume fraction of graphite. It is clear that the volume fraction of graphite/ γ is much lower at the beginning. At the end of the process it gets closer to the ideal value given by the phase diagram.

Inconel 625

The microstructure observed in the quench-out samples indicates that there is a coarsening process of the dendritic structure (figure 2.3b). Three different phases are found apart from primary austenite and liquid, NbC carbides, eutectic-like Laves and TiN precipitates. Measurements of the distribution of these phases are presented as function of the cooling rate in figure 2.5. In this case the cooling rate of the DTA samples is 0.1 K/s, the mirror samples 100 K/s and the levitation samples 10^4 K/s. The total amount of secondary phases found in the samples is lowest in the levitation samples, followed by the mirror furnace samples and the DTA samples. This behavior is related to the previous observations made about segregation

in the material. It is known that solutes which segregate strongly will end up as part of a secondary phase. Thus it is expected that the more this solute is segregated the larger the amount of secondary phase that will precipitate.

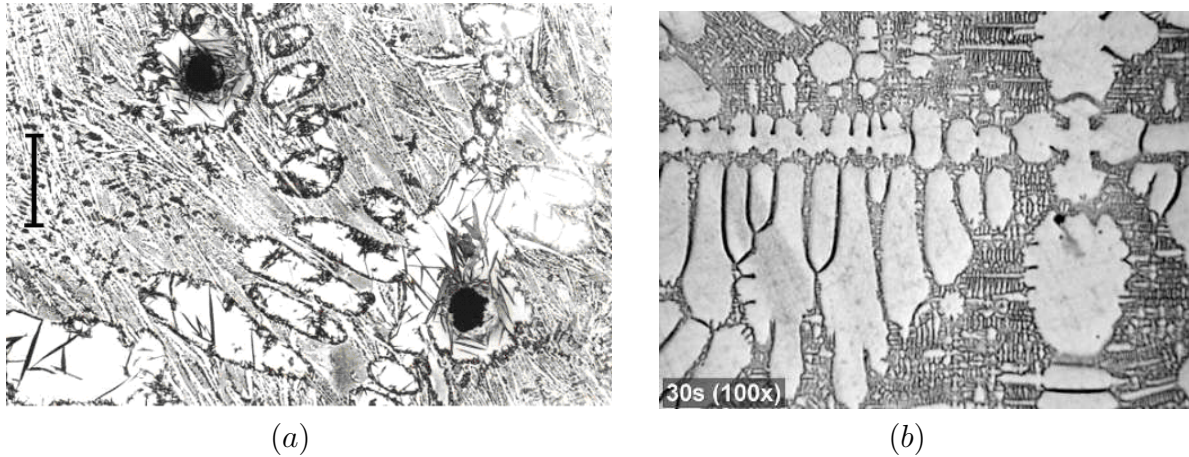


Figure 2.3: Microstructure observed in (a) nodular cast iron and in (b) Inconel 625 during solidification

2.2.3 Structure evolution

The microstructure of a metal can be characterized by means of several aspects such as: dendritic arm spacing, cell size or eutectic inter-cellular spacing. In this section a brief description of the microstructure observed in the material is presented.

Cast Iron

In nodular cast iron the graphite is formed in the melt, grows freely in the melt to a certain size, and is later surrounded by an austenite shell. The growth is then continued by diffusion through the austenite shell. The growth mechanism is very different from the one in flake graphite cast iron, where both austenite and graphite grow side by side into the liquid. The number of nodules and their size provide a notion of the evolution of the solidification in the material. In nodular cast iron an increase in the number of nodules with the cooling rate is observed (figure 2.6). This might be caused by an increase in the nucleation rate.

Inconel 625

In the case of inconel 625 the primary phase grows dendritically (figure 2.3b) and it is followed by the precipitation of secondary phases in the interdendritic regions. The secondary dendrite arm spacing (SDAS) provides a description of the dendritic growth during solidification and its behavior under different cooling rates. In Ni-base alloys the dendritic structure tends to become finer as the cooling rate increases (figure 2.7).

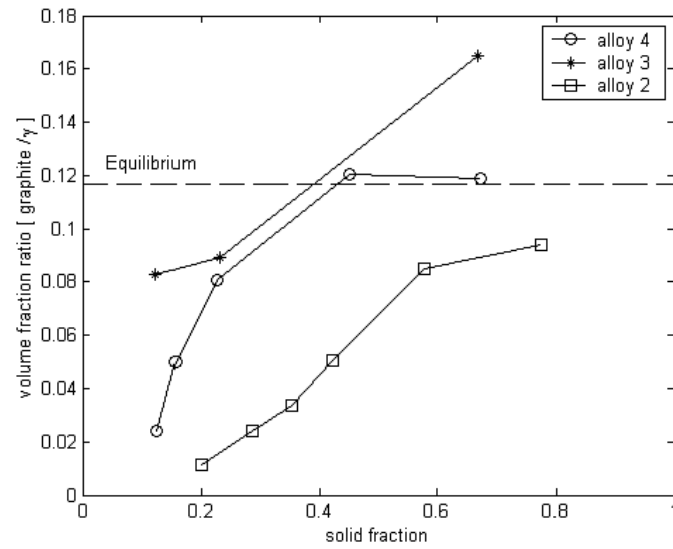


Figure 2.4: Volume fraction ratio (graphite/ γ) as function of solid fraction

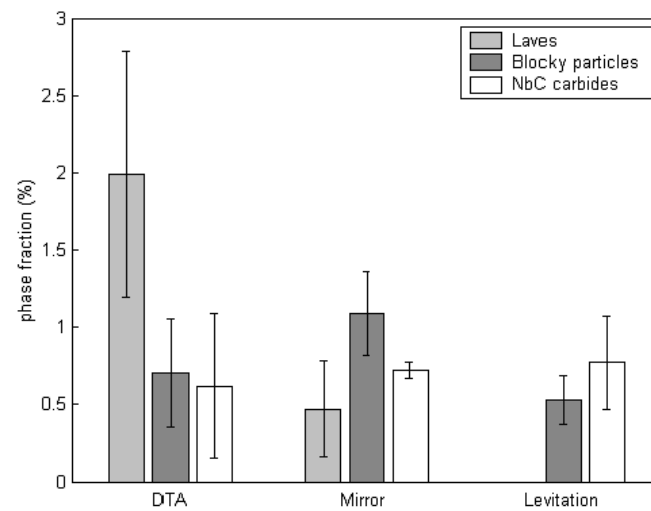


Figure 2.5: Phase volume fraction measured in Inconel 625

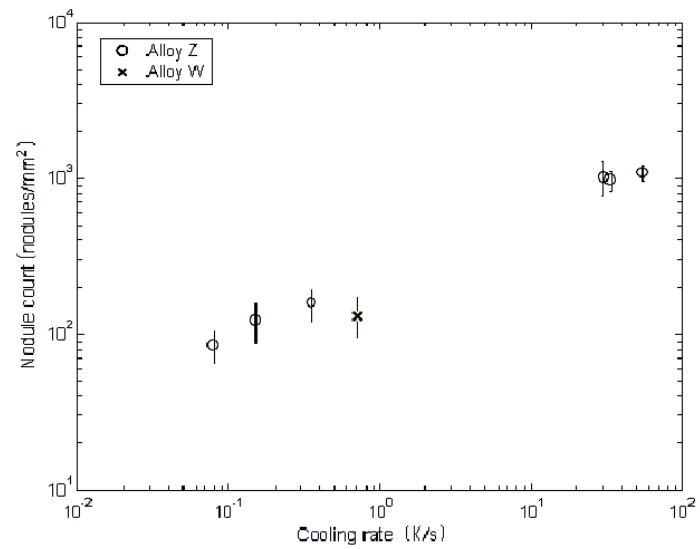


Figure 2.6: Effect of cooling rate on nodule count

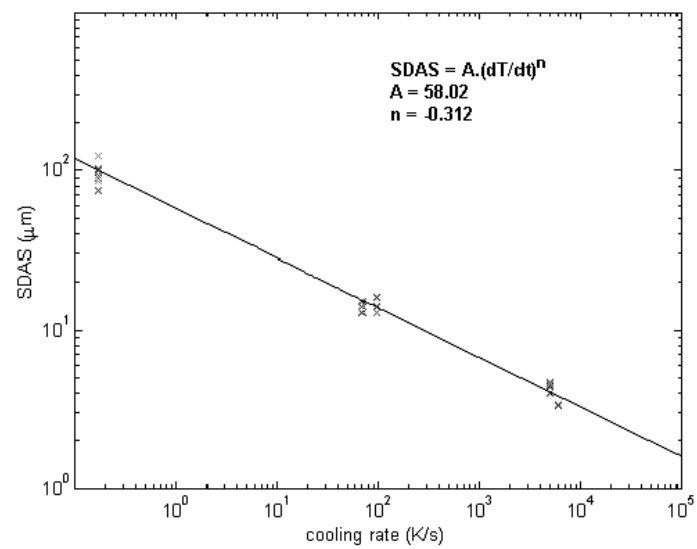


Figure 2.7: Effect of cooling rate on SDAS

Chapter 3

Heat of fusion

3.1 Heat transfer model

The theoretical analysis of the solidification process is often performed by a combination of heat transfer and crystal growth since it is possible to record the heat evolution during the process. The total amount of heat contained in the metal and the crucible is assumed to be the amount of heat transferred to the surroundings. In the DTA experiments the temperature of the surroundings is represented by the temperature of the graphite ring (figure 2.1(a)). It is further assumed that the crucible is isothermal and has the same temperature as the sample. The heat contained in the sample and the latent heat of solidification is then the heat transferred which can be expressed in terms of convection and radiation [17]:

$$Ah(T_s - T_g) + A\sigma\epsilon(T_s^4 - T_g^4) = (m_s C_{p_s} + m_c C_{p_c}) \frac{dT}{dt} + m_s \Delta H \frac{df_s}{dt} \quad (3.1)$$

where: A : sample area, h : heat transfer coefficient, σ : Stefan-Boltzmann constant, ϵ : emissivity, $m_{s,c}$: sample and crucible mass, $C_{p_{s,c}}$: sample and crucible heat capacity, $\frac{dT}{dt}$: sample cooling rate, ΔH : latent heat of fusion and $\frac{df_s}{dt}$: solidification rate. The left hand side of equation 3.1 represents the heat transfer from the crucible to the graphite while the right hand side represents the heat evolved in the crucible. By simplifying the right hand side of equation 3.1 it is possible to get:

$$Ah(T_s - T_g) + A\sigma\epsilon(T_s^4 - T_g^4) = C_{fit}(T_s - T_g) \quad (3.2)$$

C_{fit} is evaluated from the experimental data where no solidification occurs according to the following expression:

$$C_{fit}(T_s - T_g)|_{nosolidification} = (m_s C_{p_s} + m_c C_{p_c}) \frac{dT}{dt}|_{nosolidification} \quad (3.3)$$

By combining equation 3.1 to 3.3, it is possible to evaluate the latent heat as function of time. In the case of the DTA experiments C_{fit} is assumed to be a linear function of temperature. However, since the surrounding temperature is not measured during the mirror furnace or levitation experiments a lumped capacitance method had to be used to estimate C_{fit} . In this case is calculated by fitting the experimental data to a 3rd order polynomial.

3.2 Results

Heat evolution and solid fraction

Measurements of latent heat obtained for cast iron along the solidification are presented in figure 3.1. One particularly striking feature is the difference in latent heat release per unit mass between alloys with nodular graphite (alloys Z and W) and that with flake graphite (alloy Y). This difference can be explained in terms of lattice defects formed in the solid phase during the growth of the graphite nodules (supplement 3).

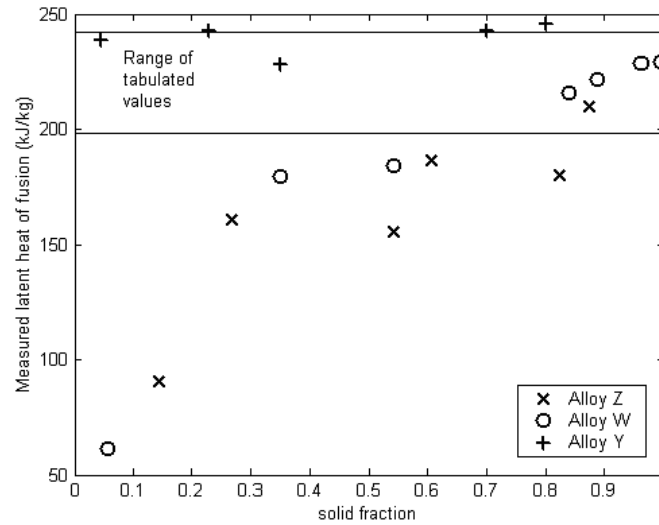


Figure 3.1: Measured latent heat of fusion as function of solid fraction

Heat evolution and cooling rate

If lattice defects are formed at the solid/liquid interface, high growth rates will promote the formation of a larger amount of lattice defects compared to slow rates. Consequently, an increase in cooling rate will encourage defect formation. This can be observed in figure 3.2 which shows how latent heat measurements decreases as cooling rate increases for Inconel 625.

3.3 Advantages and disadvantages

It is worth mentioning some of the pros and cons of this approach. Among the advantages is the possibility to measure heat release during solidification, the results can be directly compared with microstructure features and the effect of other variables such as cooling rate can also be studied. In spite of those benefits there are a series of drawbacks. Among them it must be included the uncertainty in the estimation of the heat transfer coefficient and the heat capacity change in the sample. Changes in the heat transfer coefficients due to the formation of a air gap between the metal and the crucible are difficult to estimate [18]. Temperature gradients within the sample might represent another source of uncertainty even though the sample size is chosen small to keep any gradient minimal.

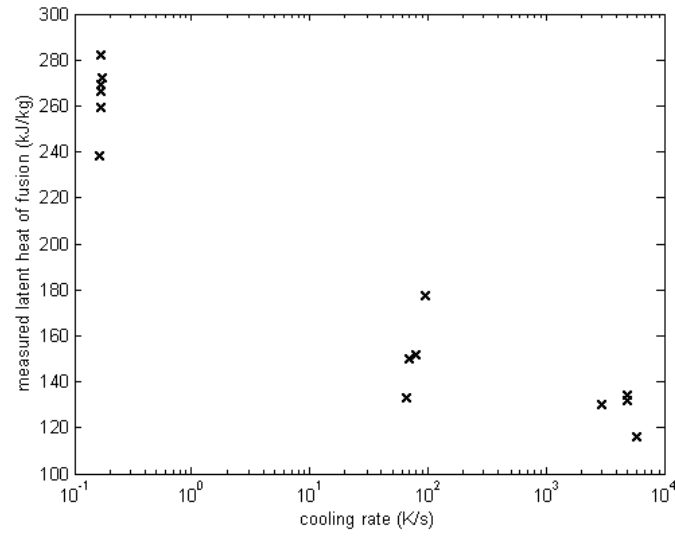


Figure 3.2: Measured latent heat of fusion as function of Cooling rate

Additionally, changes in the microstructure during the quenching operation might represent an issue sometimes not considered during analysis of the structure [19]. In this work estimations of the cooling rate during the quenching operation indicated that the levels achieved were high enough to promote the transition from stable to metastable in cast iron so a clear contrast between the two structures (solid and liquid quenched) was always obtained.

Chapter 4

Volume change and porosity

4.1 Thermodynamic considerations

Two types of shrinkage pores have been observed in nodular cast iron. One type is formed by the shrinkage during the initial period of the solidification process [10] and the other type of pores is formed at the end of the solidification. This kind of pores is known to cause a contraction at the end of the solidification process resulting in shrinkage pores.

The difference in growth mechanism between nodular cast iron and flake cast iron give rise to a difference in solidification shrinkage or expansion. It is well known that nodular cast iron needs larger risers than flake graphite cast iron with similar carbon content. It was early shown both experimentally and theoretically [8] [9] that as soon as the carbon content gets above 3.8 wt pc carbon for a binary alloy the larger specific volume of graphite compensates the smaller specific volume of austenite so that the specific volume of austenite and graphite in the eutectic structure gets larger than the one in the liquid. Then, shrinkage pores may not be formed.

Figure 3.1 illustrated that the latent heat varied with the growth mode of graphite. A decrease of the latent heat with the cooling rate is related to the number of lattice defects formed in the solid during the solidification process. The energy of the solid will thus be larger than under equilibrium conditions. Thermodynamic calculations based on a previous presented study [4] were performed in the Fe-C-vacancies system. A detailed description of this calculations is presented in supplement 3. The measured volume fraction in the samples indicated that the volume ratio $graphite/\gamma$ was lower than the predicted by the equilibrium phase diagram. In thermodynamic terms there are two possible ways to change the volume fraction ratio $graphite/\gamma$, either the graphite liquidus line in the phase diagram moves towards higher carbon contents or the austenite solidus line move towards higher carbon contents. In the first case an increase in the free energy of graphite can be achieved by increasing its vacancy concentration. An example of this case is presented in figure 4.1.

The second case is illustrated by changing the interaction coefficient between lattice defects and carbon in austenite so the carbon solubility in austenite increases. Carbon is an interstitial soluble element in austenite and an increase of the number of lattice defects reduces the density of the phase. The extra free volume can then give a possibility for more carbon to be dissolved into the austenite. This is presented in figure 4.2. In this case both the fraction of vacancies and the interaction parameter between carbon and vacancies were increased.

By means of a heat balance it is possible to estimate the fraction of vacancies formed from the latent heat measurements.

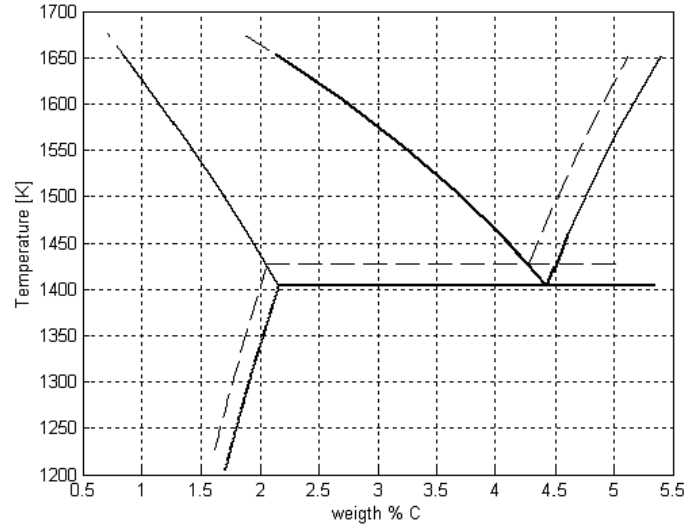


Figure 4.1: Calculated Fe-C-V phase diagram $X_{v^{\gamma}} = X_{v^{\gamma}(eq)}$, $X_{v^{graphite}} = 0.003$

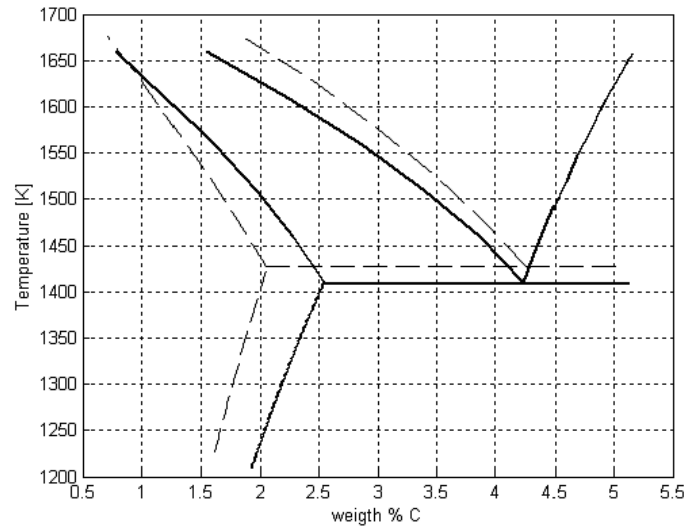


Figure 4.2: Calculated Fe-C-V phase diagram $X_{v^{\gamma}} = 0.009$, $X_{v^{graphite}} = X_{v^{graphite}(eq)}$, in this case L_{CV} was increased 15 pc

$$\Delta H_{nc} = \Delta H_{tab} - (X_V - X_V^{eq})\Delta H_V \quad (4.1)$$

where: ΔH_{nc} is the measured latent heat of nodular cast iron, ΔH_{tab} is the tabulated value of latent heat and $(X_V - X_V^{eq})$ is the difference in mole fraction of vacancies between nodular cast iron and grey cast iron. The heat balance given by equation 4.1 can be used to calculate the fraction of vacancies formed. By using the data presented in figure 3.1 about the latent heat the resulting fraction of vacancies lies between 0.05 and equilibrium.

The volume fraction ratio between graphite/ γ calculated from figures 4.1 and 4.2 indicates that the largest effect is given by an increase of the carbon content in the austenite due to an increase in the number of lattice defects (figure 4.2). A comparison between the calculated phase diagram and the experimental results (figure 5.5b) shows that the experimental observations can only be described by the case where the carbon solubility increases in austenite.

4.2 Growth rate

Calculations of the growth rate $\frac{dR}{dt}$ as function of nodule size were then performed according to equation 4.2 which takes into account the diffusion of carbon and the effect of the vacancies.

$$\frac{dR}{dt} = \frac{\left[\frac{X^{\gamma/L}}{X^{\gamma/graphite}} - 1 \right]}{R^2 \left[\frac{1}{R} - \frac{1}{S} \right] \left[\frac{1}{nD_v^{\gamma}} + \frac{V^{graphite}}{V^{\gamma}} \frac{(X^{graphite} - X^{\gamma/graphite})}{D_C^{\gamma}} \right]} \quad (4.2)$$

where $X^{\gamma/L}$ is equilibrium concentration of carbon in austenite in contact with liquid, $X^{\gamma/graphite}$ is equilibrium concentration of carbon in liquid in contact with austenite, D_v is the diffusivity of vacancies and D_C^{γ} the diffusivity of carbon in austenite, $V^{graphite}$ is the molar volume of graphite and V^{γ} is the molar volume of austenite. A material balance can be used to obtain a relation between R and S in order to estimate the effect of different parameters on the growth process. Different curves are presented in figure 4.3. The n parameter is a structural dependent constant which varies between 10 and 40. The figure shows that at high n values (close to 100) the growth rate becomes independent of n . The growth process is in this case controlled by the diffusion of carbon through the austenite shell. The conclusion here will thus be that the process is controlled by the deformation of the austenite shell.

The graphite is nucleated in the melt between the dendrites arms and it grows freely in the melt until it reaches a certain size. It was proposed by Wetterfall et al [20] that the shell is formed when the graphite nodules gets contact with the austenite due to its flotation. However, this seems to be a too simple explanation. It has been observed that the graphite nodules can have contact with austenite without being covered. The reason for this might be the fact that the growth behaviour is such that graphite and austenite have the same chemical potential, which is necessary for the growth of austenite around graphite. The difference in chemical potential can be due to the plastic deformation of the austenite.

However, this can also be an effect of the interface kinetics when graphite is precipitated from the liquid. This reaction can also produce lattice defects in the graphite which change its chemical potential during the growth. When the nodules are small the growth rate will be large and the interphase kinetics will be large. In this case it will not be possible to establish a growth of austenite around the graphite. The remaining driving force will also be too small to cause the plastic deformation of the austenite. This can then be established when the nodules

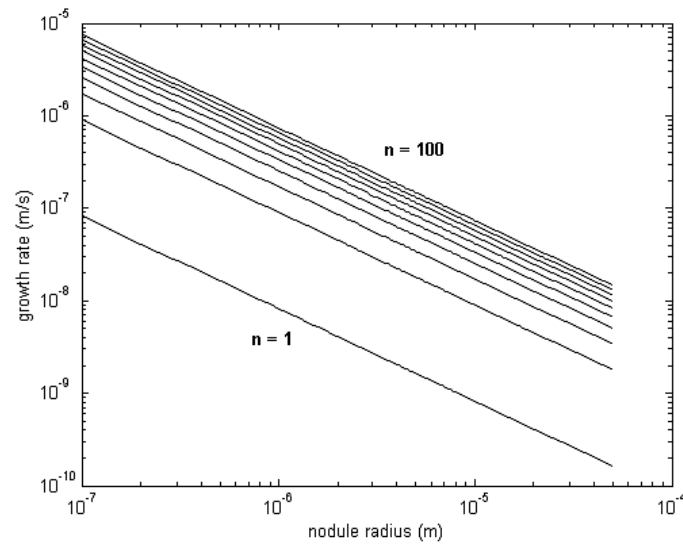


Figure 4.3: Nodule growth rate as function of its radius calculated according to equation 4.2

has reached a certain size. In the cases where austenite shells are formed the growth rate of graphite nodules decreases and the interface kinetics for growth of graphite is decreased further on.

When the growth of austenite ceases the vacancies start to condense at the same time as the graphite starts to grow due to the decrease of the carbon content in the austenite. The remaining vacancies will now condense. At this process the austenite will shrink, pores are formed. Those pores can be filled with liquid if they are in contact with the liquid or will remain in the structure as shrinkage pores.

Chapter 5

Spray forming

5.1 Plant trials

In this chapter the spray forming process will be introduced and its main features will be treated. The technology of spray atomization and deposition was pioneered during the 1970s by Singer at the University College of Swansea [21]. Nowadays it is used to produce a variety of near-net-shape preforms. In spray forming metal is atomized using high velocity gas, usually nitrogen or argon. The spray formed is deposited onto a substrate and a near-net shape is formed. The atomization of the melt creates a spray consisting of droplets with a variation in size. The variation of size causes the droplets to be in different states as they hit the substrate, i.e. liquid, mushy or solid. A schematic description of an industrial facility for spray forming of tubular preforms is presented in figure 5.1. During spray forming processing the solidification of the metal occurs over wide range of cooling rates. The solidification of the droplets in the spray occurs under high cooling rates [22] while the solidification at the deposition surface, after the droplets have impinged occurs at a much lower rate [24].

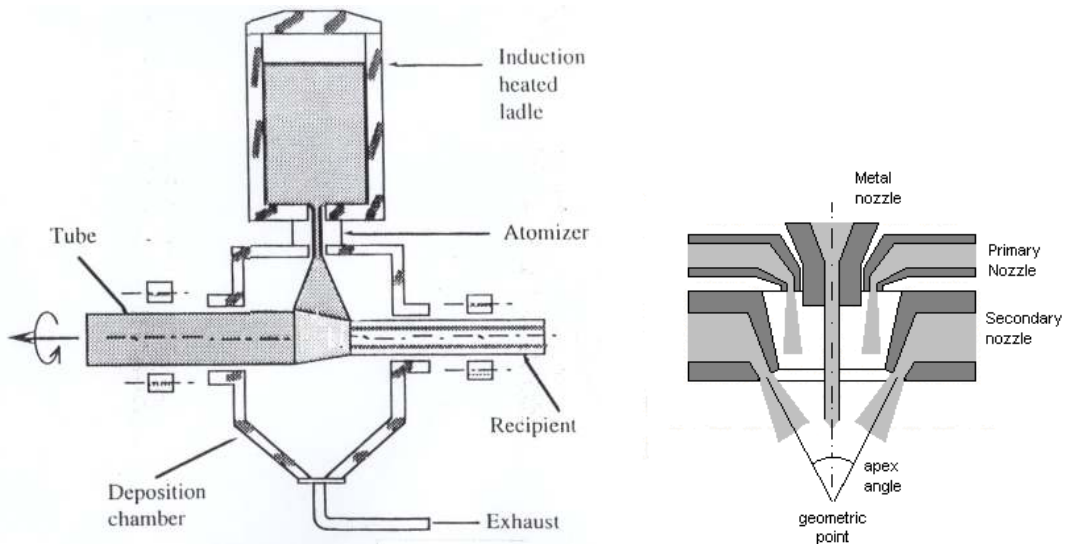


Figure 5.1: (a) Deposition chamber (b) Atomizer

It is known that convection plays a major role in the heat transfer droplet-gas taking place in the spray. The assessment of the heat transfer conditions demands knowledge about

Table 5.1: Process parameters

<i>Test</i>	1 (702055)	2 (702056)	3 (702057)
<i>Metal flow (kg/min)</i>	75	75	75
<i>P_{secondary} (bar)</i>	5.3	6.3	6.3
<i>Gas to metal ratio</i>	0.30	0.35	0.35
<i>Rotational velocity (RPM)</i>	83	90	78
<i>Axial velocity (mm/s)</i>	10.4	10.4	10.4
<i>Flight distance (mm)</i>	514	514	514

the momentum transfer between the gas and the droplets. It becomes confusing to refer to the metal as liquid droplets or as solid particles since they undergo transformation during their flight. In the following discussion both will be referred to as particles.

In order to evaluate the features describing the heat transfer conditions during spray forming, a series of experiments were carried out in an industrial facility at Sandvik Materials Technology AB where cylindrical preforms are produced. The working parameters used for the experiments are included in table 5.1. A modified version of Inconel 625 was sprayed over steel bars of 170 mm of diameter and 8 meters in length. The deposit thickness reached between 15 and 20 mm approximately.

5.1.1 Flow assessment

Different techniques can be used to investigate gas flows, i.e. Laser Doppler Velocimetry (LDV), hot wire anemometry, pitot tube, etc. Due to its reliability and robustness, the pitot tube technique represents a valuable tool for the investigation and measurement of gas flows. In this study stagnation tubes were used as the measuring technique to evaluate the flow. This was achieved by obtaining several pressure profiles at different distances from the nozzle in the same experiment. A computer-controlled linear motor was used to change the position of a carriage, where the probes were mounted, along a track in a systematic manner. In total 5 tubes were used and separated 50 mm from each other on the carriage to avoid mutual perturbations. Each tube had a different height with respect to the nozzle exit, according to figure 5.2. Plastic hoses were used to connect the probes to previously calibrated pressure transducers which provided an analog voltage signal. The pressure signals were then recorded by a computer using 2 Hz sampling rate.

In figure 5.3 the pressure measurements along the vertical axis as function distance from the atomizer are presented. As it is observed the pressure shows a maximum and then decreases as the distance to the nozzle increases. Higher levels of dynamic pressure were observed when the primary atomizer (figure 5.1b) is not active compared to the case when the primary atomizer is active.

5.1.2 Particle state analysis

Information about the particles was obtained from samples of overspray powder collected after each deposition. Sieving analysis performed on powder samples determined the particle size distribution. Selected particles from sieved samples were metallographically prepared by mounting in transparent resin, grinding and polishing. The microstructure was revealed by

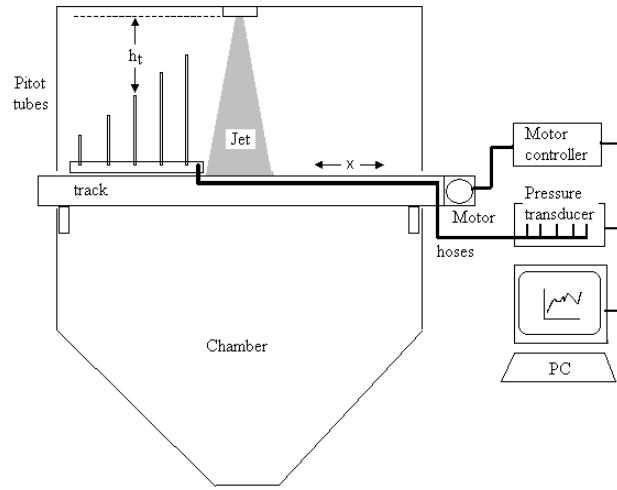


Figure 5.2: Experimental set up for gas velocity measurements

etching with a solution of 3 parts HCl with 1 part HNO_3 . Measurements of the SDAS were performed. Additionally, by studying metallographic samples of the deposit a number of embedded particles were also evaluated. Results showed that SDAS is proportional to the particle diameter (figure 5.4). By using the material solidification characteristics previously described (figure 2.7), a determination of the cooling rate under which the particles did solidify was made.

5.1.3 Structure in the deposit

The main defining feature found in the microstructure of the spray deposited material was a fine equiaxed grain structure. A detailed evaluation of the deposit samples indicated three distinguishable zones as they appear from the substrate; a porous and dendritic zone, a transition zone and an equiaxed zone. During the evaluation of the samples, a gap between the substrate and the deposit was always found. The length of the equiaxed zone represented two thirds of total thickness of the deposit. Figure 5.5 shows the typical microstructure observed in the equiaxed zone. In this region the average grain length intercept varies between $30\ \mu m$ and $50\ \mu m$.

Porosity

Results from the porosity measurements are presented in figure 5.6. As it is possible to observe in the figure, as the thickness of the deposit increases the porosity decreases sharply. Near the substrate the porosity reaches up to 12 percent and then it decreases to rather low levels ($< 0.5\ pc$). It is also observed than a relative increase in porosity is registered at the top of the deposit.

5.2 Numerical simulations

In this section it is presented a modelling study of the spray casting process. In order to facilitate the analysis it is helpful to separate the process into two distinct but closely related

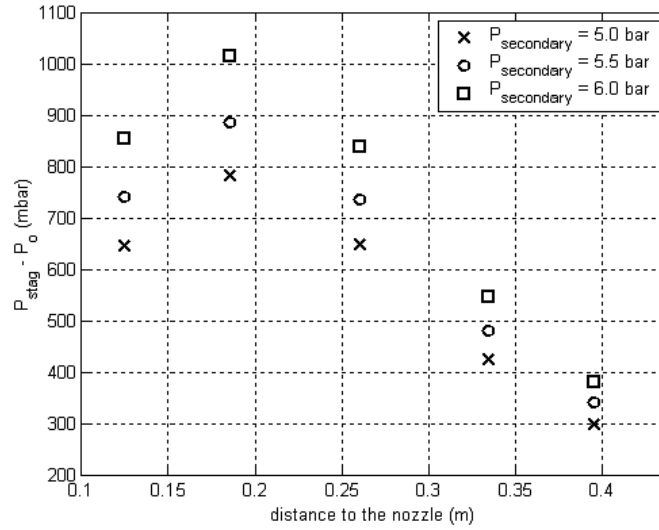


Figure 5.3: Measured dynamic pressure at the spray axis

stages. The first stage consists of those phenomena that are primarily active in the spray prior to impingement onto the substrate. The second stage begins after the droplets have impinged on the deposition surface [25]. The present understanding of the phenomena involved in both stages of the spray forming process is still not fully satisfactory from the point of view of both experimental study and theoretical modelling [26]. Even though it is during the second stage that the deposit microstructure is formed it is necessary to address the parameters governing the first stage as a starting point.

In addition to the knowledge of the state of the spray, modelling of the heat transfer to and from the deposit is required for the prediction of the fraction of liquid on the top surface of the deposit and thus the structure evolution. Two basic types of models, continuum and discrete, have been developed to describe the thermal and solidification history during the interaction of droplet with the substrate, particularly for temperature distribution and solidification time [27] [28]. In the continuum model, the behavior of the individual droplets is considered at an average scale of all droplets in the spray, whereas in the discrete models the behavior of individual droplets is investigated separately. In this section a description of a continuum-type model is presented together with some of the results obtained.

5.2.1 CFD model

Computational fluid dynamic (CFD) modelling was used to describe the events occurred during the in-flight. The fluid dynamic model is developed by solving the Navier-Stokes equations for conservation of mass and momentum for different flow conditions. The flow is solved by assuming that it is turbulent, compressible and developed into a steady state condition. The basic set of equations, solved by a commercial program *CFX* version 4.4, comprises equations for the conservation of mass and momentum. In a non-isothermal flow, the first law of thermodynamics provides an equation for energy. The equations are presented in a Cartesian coordinate system [23]. The particle transport was modelled by using a Lagrangian approach, in this case the added droplets are tracked throughout the computational space. The fully coupled calculations are performed by solving the set of partial differential equations for the flow and then

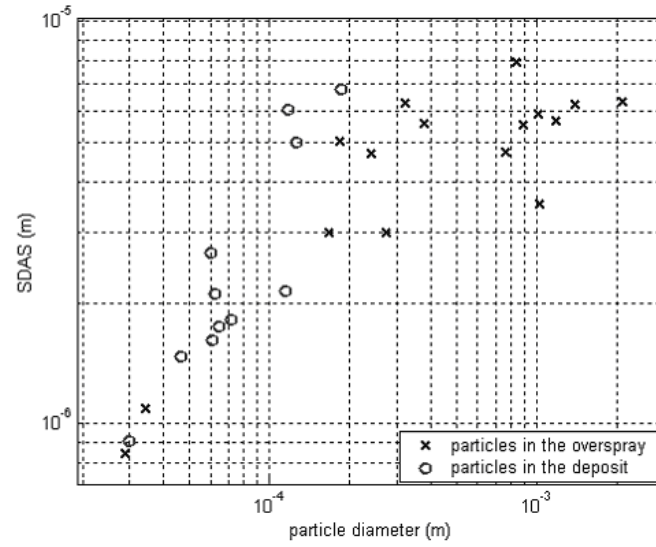


Figure 5.4: Secondary dendrite arm spacing measured in the particles

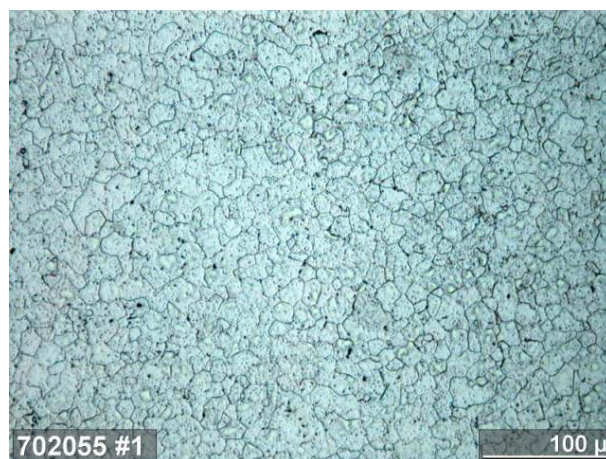


Figure 5.5: Typical microstructure found in the deposit

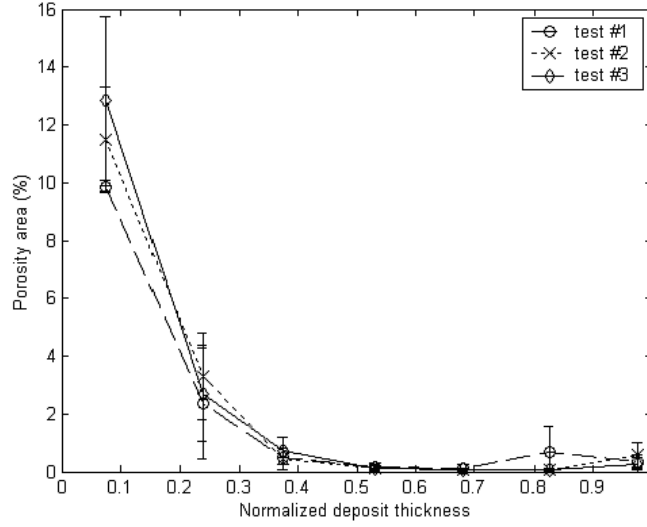


Figure 5.6: Porosity found in the deposit as function of distance to the substrate

the particle transport ordinary differential equations are solved as an outer loop. A detailed description of the model is given in supplement 5. The solidification of the particles is taken into account by using a heat capacity variable in the droplet;

- if $T > T_{liq}$ $Cp = Cp_{liq}$
- if $T_{liq} > T > T_{sol}$

$$Cp = Cp_{sol} + (\Delta H \frac{df_s}{dT}) \quad (5.1)$$

- if $T_{sol} > T$ $Cp = Cp_{sol}$

where; $Cp_{liq,sol}$ represent the particle heat capacity in the liquid and solid state, $T_{liq,sol}$ represent the liquidus and solidus temperature, ΔH represents the latent heat of fusion and $\frac{df_s}{dT}$ is given by the solidification model used, in this case the lever rule.

Domain

A structured mesh was used in both 3-D and 2-D calculations. A grid independence study was use to analyze the suitability of the mesh and to estimate the numerical error in the simulation [29]. Three significantly different grids were used. Additionally, selective local refinement was applied in critical flow regions of the domain as for example the atomization region.

Boundary conditions

- **GAS INLET:** It was assumed as an annular manifold where pressure, temperature and relative turbulence intensity are defined. In order to facilitate the implementation of the particle transport model a special inlet was used, similar approaches has been reported previously [22].

- **METAL INLET:** Particles were introduced at the atomization region. Particle diameters, as well as their number, were defined by a Rosin-Rammler distribution. The particle size distribution (PSD) parameters were defined according to the experimental information obtained from powder analysis. A superheat of 100 K was chosen for the particles.
- **CHAMBER WALLS:** Free slip condition was set on this boundary. The temperature was set according to the temperature levels reached in the real chamber around 350 K.
- **OUTLET:** Atmospheric pressure was assumed at this boundary. The temperature was varied between 290 K and 540 K so that information about the effect of the temperature of the gas in the chamber could be obtained.

Convergence

The default convergence criterion for the CFX flow solver is when the mass source residual has reached a sufficiently small value set by the user. The mass source residual is defined as the sum of the absolute values of the net mass fluxes into or out of every cell in the flow. For the present case, the iterations were stopped when all residuals were reduced to some final value between 10^{-3} and 10^{-6} and the mass source residual had reached about 10^{-5} . The two-way coupled calculations were assumed to be converged after 10-20 iterations of the outer loop.

Gas flow results

Calculations performed on the entire chamber help to understand and localize the areas of interest for further study. By taking advantage of the symmetry in the geometry only one half of the real chamber was simulated. Due to the structured character of the grid some distortion had to be accepted in this case. A simple opening was used as a first approach to the real atomizing nozzle (figure 5.1b). Figure 5.7 presents the gas velocity results from 3-D calculations. It is possible to observe a high velocity region in the upper half of the chamber.

This observation partly indicates that the top part of the chamber is the critical section of the flow. To reduce computational effort 2-D axis-symmetric calculations were then performed. In this case no substrate was included in the calculations. A pressure boundary was used to define the limits of the domain which did not correspond to the chamber walls. Figure 5.8 presents the velocity field in the upper part of the chamber when the pressure in the atomizer is 5.5 bar. In this figure it is possible to observe how the gas is accelerated when it passes through the nozzle exit, reaching velocities close to Mach 1. Once the gas leaves the nozzle the velocity decreases rapidly, an expected behavior for a free jet. In this case the flow reaches velocities close to Mach 0.8 in the vicinity of the atomization region.

5.2.2 Deposition

A schematic representation of the deposition process is presented in figure 5.9. A finite difference method is used to solve the heat transport equation in the radial direction for a time interval equivalent to a revolution.

Domain

A 1-D grid is extended each revolution after a new layer of sprayed material is added. Constant mass or thickness increase is assumed after each revolution. This procedure is repeated until the deposition is completed and prolonged a number of revolutions. In order to account for the

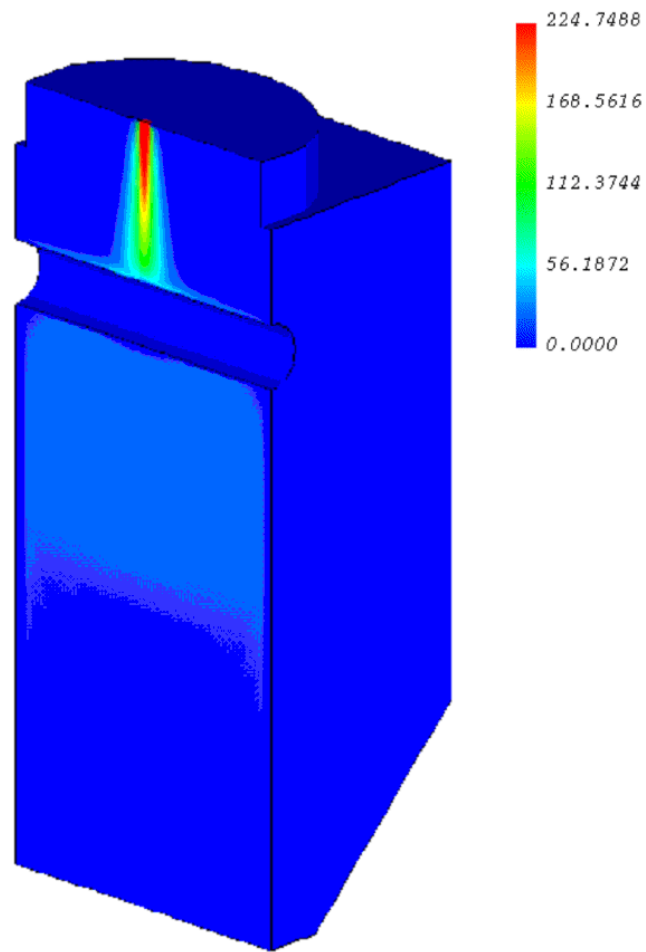


Figure 5.7: Gas velocity results obtained from 3-D calculations

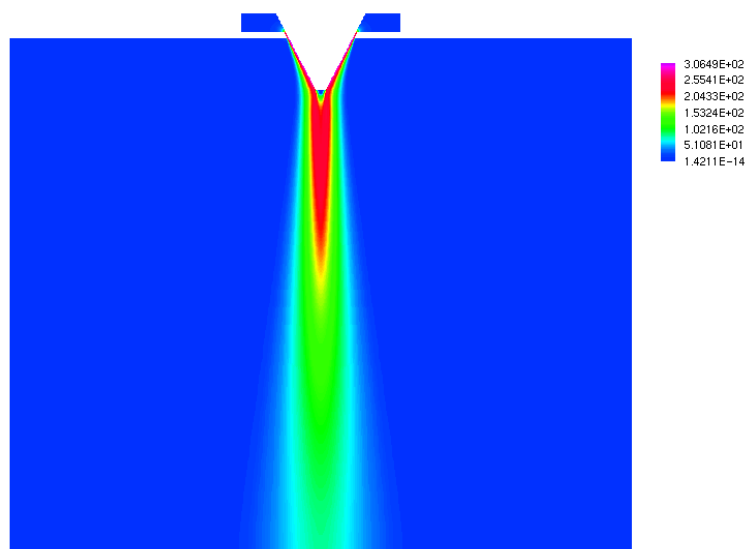


Figure 5.8: Gas velocity results obtained from 2-D calculations.

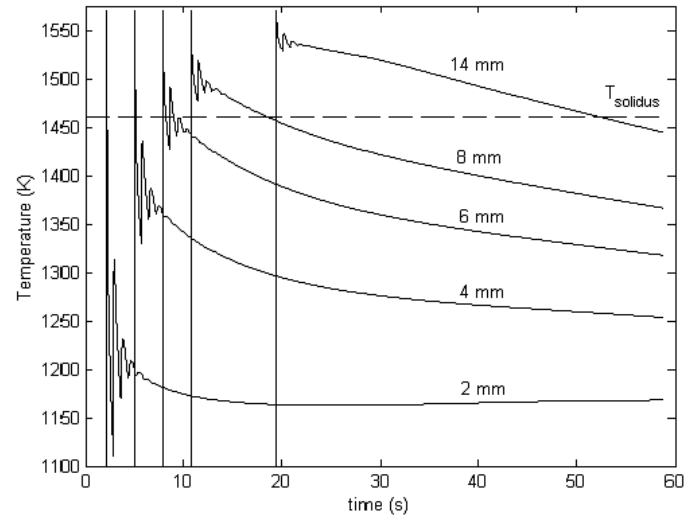


Figure 5.10: Thermal history of the deposit

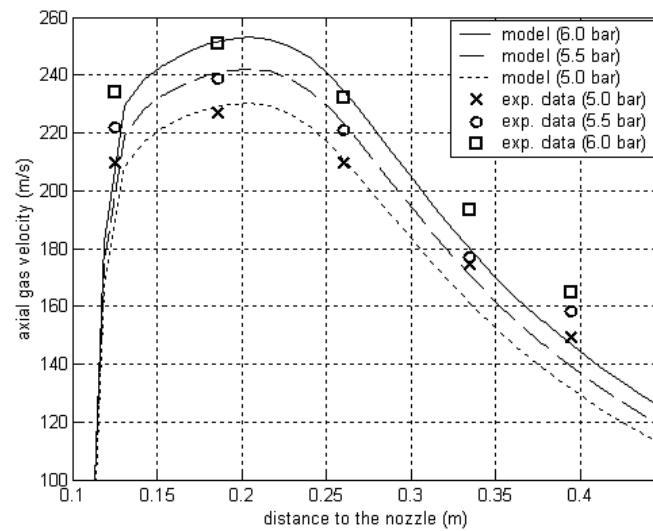


Figure 5.11: Gas velocity at the axis as function of the distance to the nozzle

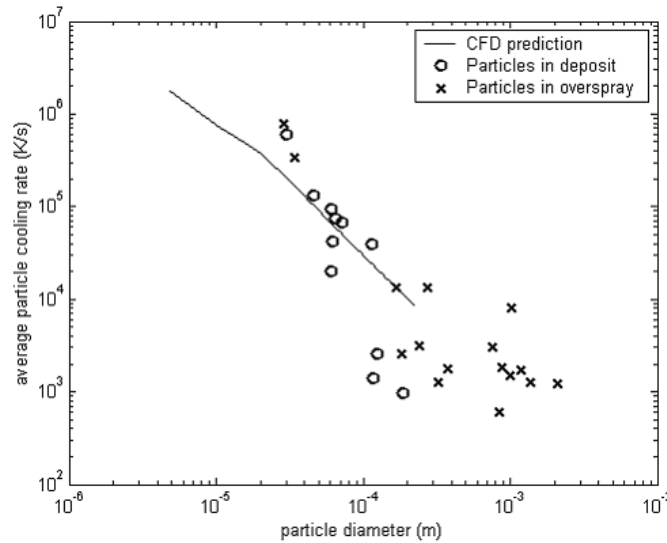


Figure 5.12: Particle cooling rate in the spray

In figure 5.12 the estimated cooling rate before solidification for each particle measured is presented. In this figure the CFD prediction is also presented. The CFD model predicts well for medium particle diameters, i.e between 50 and 100 μm .

The structure coarseness is related to the solidification time by the relationship presented in figure 2.7. It is suggested that the structure solidified within a time interval between 10 and 40 sec. The results from the deposition simulations also indicates that the solidification time of the deposit is in that range (10-50 s). This can be illustrated by presenting the experimental data together with the predictions from the deposition model in terms of the structure coarseness. In this case the feature describing the structure coarseness is the average grain length intercept (figure 5.13)

Taking into account the range of solidification time it might be expected that the segregation in the deposited material would be something in between that found in the mirror and in the DTA samples. Surprisingly, the minimum concentration measured is lower than the registered for the levitation samples. This indicates that there is a mechanism of chemical homogenization taking place in the material during the process. The range of cooling rates which takes place during the in-flight will affect the solidification process in a number of aspects, such as:

- The decrease in the latent heat of fusion
- The amount of material transformed
- The segregation behavior

The decrease of heat of transformation can also be interpreted as a delay in the liberation of the latent heat, in other words the energy suppressed during the in-flight will be added to the energy released during the solidification at the substrate. By performing a calculation on the temperature evolution in the deposit, it was found that an increase of 50 percent in the latent heat does not affect largely the ranges of solidification time obtained by the numerical procedure (figure 5.13). The determination of the amount of material transformed in the

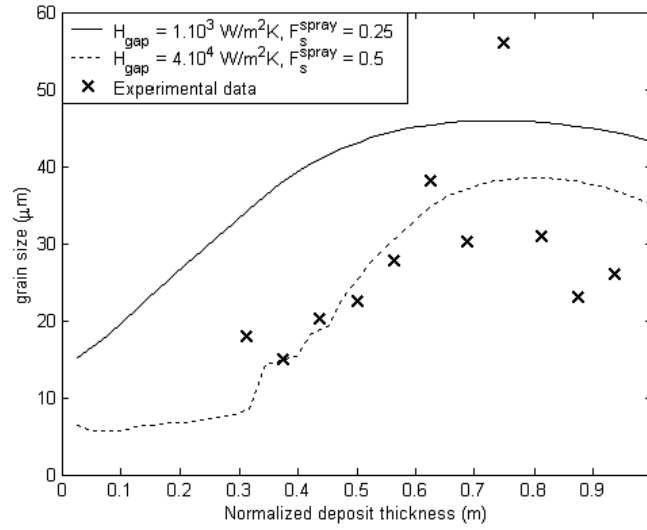


Figure 5.13: Grain size in the deposit

particles and the magnitude of thermal equilibration represents two different aspects which are combined at the surface of the deposit, estimations of one of them might disregard the other adding complexity to the problem. However the segregation behavior has proved to be a useful indicator of the conditions during the formation of the structure. The low levels of segregation are comparable to those observed in the levitation samples, i.e C_{min}/C_0 approximately 0.7 (in the case of niobium), even though the solidification time scale and structure coarseness are much larger. Then it seems that the non-equilibrium conditions occurring during in-flight left a sort of footprint on the material in terms of segregation but not in terms of structure coarseness.

Chapter 6

Concluding remarks

There are a number of ways to explain independently observations concerning the effect of cooling rate and structure morphology in solidification characteristics of a given material such as: variation of latent heat of fusion, amount of precipitated phases and segregation behavior. The presence of lattice defects during the solidification process has so far explained them altogether.

By considering the formation of lattice defects and by using conventional thermodynamic relations it is possible to describe kinetics effects in the solidification process. It has also been described by means of a validated numerical model a particular solidification process occurring in a real industrial application.

Finally the limitations of this work include among others; first the issues dealing with heat transfer measurements and second the considerations in the two-phase flow calculations dealing with the coupling gas-particles. Further work needs to be done to develop better heat transfer measurements during thermal analysis. These findings suggest several courses of action for controlling porosity in castings in the systems and process considered.

Bibliography

- [1] B. J. Hribovsek and B. Marincek, The Metallurgy of Cast Iron, Ed. B Lux, 659-672 (1974)
- [2] S. Berg, J. Dalhström, H. Fredriksson, ISIJ International Vol. **35**, 876-885 (1995)
- [3] H. Fredriksson, Advanced Materials Research, Vol. **4 — 5**, 505-512 (1997)
- [4] T. ElBenawy, H. Fredriksson, Mat. Transactions, JIM, Vol **41**, No 4, 507-515 (2000)
- [5] J. Mahmoudi, H. Fredriksson, Materials Science and Engineering A, Vol. **22A**, 226-228 (1997)
- [6] H. Fredriksson, T. Emi, Materials Transactions, JIM, Vol. **39**, No.2 (1998) 292-301
- [7] I. Minkoff, The physical metallurgy of cast iron, 1st edition, (1983)
- [8] W.A. Schmidt, H.F. Taylor, AFS Transactions, Vol. **43**, 131-141 (1953)
- [9] W.A. Schmidt, E. Sullivan, H.F. Taylor, AFS Transactions, Vol. **9**, 70-77 (1954)
- [10] D.M. Stefanescu, H.Q. Qiu, C.H. Chen, AFS Transactions, Vol. **57**, 189-197 (1995)
- [11] R. Hummer, Mat. Res. Symp. Proc, Elsevier Science Pub, Vol. **34**, 213-222 (1985)
- [12] W. Cai, E. Lavernia, Metall. Trans. B., Vol. **29B**, 1085-1096 (1998)
- [13] W. Cai, E. Lavernia, Metall. Trans. B., Vol. **29B**, 1097-1106 (1998)
- [14] F. Rudberg, Ann. Chim. Phys., Vol. **48**, 353 (1830)
- [15] C. Lockowandt, K. Löth, L. Ekbom, A. Eliasson, A. Jarfors: VII Europ. Symp. Mat. And Fluid Sci. Microg. ESA, Brussels, 383-386, April (1992)
- [16] T. Antonsson, On the interaction between liquid/solid during sintering and solidification, PhD thesis, KTH, Stockholm (2003)
- [17] B. Rogberg, H. Fredriksson, Metal Science, Vol. **14**, 685-690 (1979)
- [18] J. Kron, T. Antonsson, H. Fredriksson, Int. J. Cast Metals Res., Vol. **14**, 275-285 (2002)
- [19] O. Pompe, M. Rattenmayr, Journal of crystal growth, Vol. **192**, 300-306 (1998)
- [20] S. E. Wetterfall, H. Fredriksson, M. Hillert: JISI, 323-333, May (1972)
- [21] A. R. E. Singer, J. Inst. Met., Vol. **100**, 185 (1972)

- [22] Underhill R., Grant P.S., Cantor B., Bryant D.J., *Int. J. of Non-equilibrium Proc.*, Vol. **10**, No 2, 201 (1997)
- [23] CFX 4.3 Flow solver user guide, AEA technology, Harwell UK
- [24] R. Doherty, C. Cai, K. Warner, *Int. J. Powder metall.*, Vol. **33**, 50-60 (1997)
- [25] S. P. Mehrotra, *Powder Metallurgy International*, Vol. **13**, 80-84 (1981)
- [26] J. S. Zhang, H. Cui, X. J. Duan, Z. Q. Sun, G. L. Chen, *Mater. Sci and Eng. A*, Vol. **A276**, 257-265 (2000)
- [27] P. Marthur, S. Annavarapu, D. Apelian, A. Lawley, *Journal of Metals*, Vol. **42**, 23-28 (1989)
- [28] S. Annavarapu, D. Apelian, A. Lawley, *Metall. Trans. A*, Vol. **21A**, 3237-3256 (1990)
- [29] M. Casey, T. Wintergerste, Special interest group in "Quality and Trust in Industrial CFD" Best practice guidelines, ERCOFTAC, Version 1.0, (2000)
- [30] A. Bejan, *Convection heat transfer*, 2nd edition (1993)

Acknowledgements

I would like to express my sincere gratitude to:

Professor **Hasse Fredriksson** for giving me the possibility to pursue my doctoral studies under his supervision and for always trusting in my capacity.

Professor **Björn Widell** for his valuable help and supervision in the performance of the industrial study.

My dear family here in Sweden, **Heriberto, Evelina** and specially **Dalina** for supporting me during the toughest moments, and in Venezuela my mother **Evelyn Alfonzo**, my father **José Rafael Tinoco** for all the encouragement.

Professor **Omar Quintero** for his guidance throughout my years at the Universidad Simón Bolívar and for becoming a friend ever since.

Lena Magnusson and **Jonas Åberg** for offering me their friendship since the very beginning.

Ander Lagerstedt, Jenny Kron, Jessica Elfsberg, Elizabeth Lampén, Tomas Bergström, Ander Eliasson, Jonas Fjellstedt, the present and former staff at Casting of Metals division for making the days at work an enjoyable experience.

Dr. Tommy Nylén, Vice President Research and Development at **Åkers AB** for supporting part of this work.

Dr. Bo Rogberg, at **AB Sandvik Materials Technology** for supporting the industrial study.

Financial support from the Stiftelsen för Internationalisering av Högre Utbildning och Forskning **STINT**, The multiphase flow program sponsored by Stiftelsen för Strategisk Forskning **SSF** and the **Universidad Simón Bolívar** are gratefully acknowledged.

Supplement 1

J. Tinoco and H. Fredriksson,

On the solidification behavior of nodular cast iron

Proceedings of the International Conference

"The Science of Casting and Solidification",

Brasov, Rumania, 305-311 (2001)

Supplement 2

J. Tinoco, P. Delvasto, O. Quintero and H. Fredriksson,
*Thermal analysis of nodular and lamellar eutectic
cast iron under different cooling rates*

International Journal of Cast Metals Research,
Vol. **16** No. 1-3 (2003)

Supplement 3

H. Fredriksson, J. Stjerndahl and J. Tinoco,

*On the solidification of nodular cast iron
and its relation to the expansion and contraction*

ISRN-KTH: MG-INR-03:05se, TRITA-MG 2003:05

Supplement 4

J. Tinoco and H. Fredriksson

*Solidification of a modified Inconel 625
alloy under different cooling rates*

Accepted for publication in the Journal of
High Temperatures Materials and Processes, Sept (2003)

Supplement 5

J. Tinoco, B. Widell, L. Fuchs and H. Fredriksson,
Modelling the in-flight events during metal spray forming
In press in Materials Science and Engineering A, Nov (2003)

Supplement 6

J. Tinoco, B. Widell and H. Fredriksson,

*Fluid flow studies in a metal spray deposition chamber.
CFD model and validation*

Accepted for publication in
Materials Science and Engineering A, Sept (2003)

Supplement 7

J. Tinoco, B. Widell and Fredriksson, H.

Metal spray deposition of cylindrical preforms

ISRN-KTH: MG-INR-03:06se, TRITA-MG 2003:06